

# Correcting radiofrequency inhomogeneity effects in skeletal muscle magnetisation transfer maps

C. D. J. Sinclair<sup>a,b,\*</sup>, J. M. Morrow<sup>a</sup>, M. G. Hanna<sup>a</sup>, M. M. Reilly<sup>a</sup>,  
T. A. Yousry<sup>a,b</sup>, X. Golay<sup>b</sup> and J. S. Thornton<sup>a,b</sup>

The potential of MRI to provide quantitative measures of neuromuscular pathology for use in therapeutic trials is being increasingly recognised. Magnetisation transfer (MT) imaging shows particular promise in this context, being sensitive to pathological changes, particularly in skeletal muscle, where measurements correlate with clinically measured muscle strength. Radiofrequency (RF) transmit field ( $B_1$ ) inhomogeneities can be particularly problematic in measurements of the MT ratio (MTR) and may obscure genuine muscle MTR changes caused by disease. In this work, we evaluate, for muscle imaging applications, a scheme previously proposed for the correction of RF inhomogeneity artefacts in cerebral MTR maps using  $B_1$  information acquired in the same session. We demonstrate the theoretical applicability of this scheme to skeletal muscle using a two-pool model of pulsed quantitative MT. The correction scheme is evaluated practically in MTR imaging of the lower limbs of 28 healthy individuals and in two groups of patients with representative neuromuscular diseases: Charcot-Marie-Tooth disease type 1A and inclusion body myositis. The correction scheme was observed to reduce both the within-subject and between-subject variability in the calf and thigh muscles of healthy subjects and patient groups in histogram- and region-of-interest-based approaches. This method of correcting for RF inhomogeneity effects in MTR maps using  $B_1$  data may markedly improve the sensitivity of MTR mapping indices as measures of pathology in skeletal muscle. Copyright © 2011 John Wiley & Sons, Ltd.

**Keywords:** quantitative MRI; RF mapping;  $B_1^+$ ; magnetization transfer; muscle; inclusion body myositis; Charcot-Marie-Tooth disease; neuromuscular disorder

## INTRODUCTION

The potential of quantitative muscle MRI to provide outcome measures for therapeutic trials in disabling and progressive neuromuscular conditions is receiving increasing attention (1,2). One such quantitative MRI method holding promise in this context is magnetisation transfer (MT) imaging (3), where contrast depends on the relative proportions of 'free' water hydrogen protons and protons bound to macromolecules in tissue. The skeletal muscle MT ratio (MTR) has been studied in healthy subjects (4), in the context of exercise (5,6), and has been shown to be reduced in neuromuscular diseases, including peripheral neuropathies (7), dermatomyositis (8) and limb girdle muscular dystrophy (9). Moreover, in peripheral neuropathies, strong associations between muscle MTR and clinically measured muscle strength have been recorded, suggesting that MT measures may offer clinically relevant indices of neuromuscular pathology (7). In the brain, where MT has been studied extensively (3), such measures have already been adopted in clinical studies in conditions such as multiple sclerosis (10,11).

MT imaging is particularly sensitive to systematic instrumental inhomogeneities, which must be accounted for if measurements are to be reliable, sensitive and reproducible (12). In particular, variations in the radiofrequency (RF) transmit field ( $B_1$ ) of the scanner can introduce substantial spatial variation in the resulting MT parameter maps. Such effects, if not dealt with appropriately,

may artificially increase the intra- and inter-subject variability of measured values, thus reducing the apparent sensitivity of MT to genuine disease processes.

The MT effect is achieved by saturating bound water protons with an off-resonance RF pulse, and measuring the reduction in the conventional MRI signal magnitude that arises from the equilibration of the free and bound proton pools through cross-relaxation (3). Variation of the  $B_1$  field causes the applied MT saturation pulse amplitude to deviate from its nominal value, in turn yielding spatially dependent MTR values. A number of

\* Correspondence to: C. D. J. Sinclair, MRC Centre for Neuromuscular Diseases, Box 65, National Hospital for Neurology and Neurosurgery, Queen Square, London WC1N 3BG, UK.  
E-mail: c.sinclair@ion.ucl.ac.uk

a C. D. J. Sinclair, J. M. Morrow, M. G. Hanna, M. M. Reilly, T. A. Yousry, J. S. Thornton  
MRC Centre for Neuromuscular Diseases, Department of Molecular Neurosciences, UCL Institute of Neurology, London, UK

b C. D. J. Sinclair, T. A. Yousry, X. Golay, J. S. Thornton  
Academic Neuroradiological Unit, Department of Brain Repair and Rehabilitation, UCL Institute of Neurology, London, UK

**Abbreviations used:** CMT1A, Charcot-Marie-Tooth disease type 1A;  $COV_{MTR}$ , coefficient of variation of MTR; FLASH, fast low-angle shot; IBM, inclusion body myositis; (q)MT(R), (quantitative) magnetisation transfer (ratio); RF, radiofrequency; ROI, region of interest; TA, tibialis anterior.

processes influence the actual  $B_1$  field distribution, including the imaging field strength, tissue magnetic permeability, anatomical geometry and coil design. These effects can be largely accounted for by measuring the deviation from the nominal, uniform field with appropriate  $B_1$  mapping sequences and including this deviation explicitly in the analysis of so-called quantitative MT (qMT) experiments (13). However, the acquisition and analysis of qMT data can be complex and time consuming. MTR measurements, in contrast, involve fewer acquisitions and are therefore arguably more suited to the clinical environment. However, because MTR describes the relative intensities of saturated and unsaturated images,  $B_1$  variation cannot be accounted for analytically when calculating the MTR. In addition, the degree to which the  $B_1$  field influences the MTR is dependent on the relative amount of proton density or  $T_1$  weighting in the acquisitions.

In an attempt to overcome these limitations, Ropele *et al.* (14) proposed a method to correct MTR values measured in the brain retrospectively using  $B_1$  maps, by means of an idealised linear relationship between MTR and  $B_1$  deviation. This method has been shown to reduce the inter-subject variation of white matter MTR histogram properties in normal subjects and patients with multiple sclerosis, and also to eliminate significant differences between inter-site MTR values in a multi-centre study (14,15). Given the successful demonstration of this correction scheme for cerebral MTR data, it seems appropriate to investigate a similar approach to correcting MTR measurements in skeletal muscle. In order to do this rigorously, it is necessary to first verify theoretically that the method is appropriate for the particular MT properties of muscle tissue. The qMT properties of normal human skeletal muscle have been measured recently (16), thus allowing the theoretical verification of the MTR  $B_1$  correction scheme for this tissue.

In this work, we model the response of MTR to  $B_1$  variation using skeletal muscle MT parameters to assess the suitability of a scheme to retrospectively correct muscle MTR maps for  $B_1$  variations. When a correction is conducted in the brain, segmented white matter is conventionally used as a homogeneous tissue to establish a local correction factor, which is then generalised and applied to all other cerebral tissues to perform the overall correction to the MTR map (14). In this work, we segment out normal muscle regions as a tissue with theoretically homogeneous MT properties from which to derive MTR correction factors. These factors are then applied to the diseased muscle, which, for these purposes, is considered as a tissue with different MT properties. Lower limb MTR and  $B_1$  data were acquired in healthy subjects to evaluate the performance of the correction method in normal skeletal muscle. Two patient groups with representative neuromuscular conditions were also imaged to assess the applicability of the correction scheme in the presence of disease. MTR histograms and regions of interest (ROIs) were used to determine whether the proposed method can reduce instrumentally induced inhomogeneities in skeletal muscle MTR maps, a step which will be vital to facilitate the effective application of MTR as a quantitative marker of neuromuscular disease.

## MATERIALS AND METHODS

### Correction scheme for muscle MT maps

The MTR in percentage units (p.u.) can be calculated from the normalised difference between the intensity of an image

acquired with a preceding MT saturation pulse ( $I_1$ ) and an image without saturation ( $I_0$ ) via the relationship:

$$\text{MTR} = 100 \times \frac{I_0 - I_1}{I_0} \text{ (p.u.)} \quad [1]$$

The amount of MT-induced signal suppression depends on the duration  $\tau$  and nominal amplitude (flip angle)  $\theta_0$  of the applied saturation pulse. If the actual applied flip angle differs from the prescribed nominal angle as a result of  $B_1$  variations, the measured MTR will deviate from the nominal 'true' value  $\text{MTR}_0$ , resulting in an error defined here as:

$$\text{MTR}_{\text{Error}} = \frac{\text{MTR} - \text{MTR}_0}{\text{MTR}_0} \quad [2]$$

Likewise, if the actual applied flip angle  $\theta$  can be measured using a suitable  $B_1$  mapping method, the  $B_1$  error is given by:

$$B_{1,\text{Error}} = \frac{\theta - \theta_0}{\theta_0} \quad [3]$$

Using a two-pool model of the MT process, it can be shown that the magnitude of  $\text{MTR}_0$  varies in a nonlinear fashion as the flip angle  $\theta_0$  is varied (13), precluding a simple direct correction of MTR based on empirical measurements of  $\theta$ . However, based on numerical modelling of qMT in the brain, Ropele *et al.* (14) showed that there exists an idealised approximate linear relationship between  $\text{MTR}_{\text{Error}}$  and  $B_{1,\text{Error}}$  with a constant of proportionality  $k$ , expressed as  $\text{MTR}_{\text{Error}} = k \times B_{1,\text{Error}}$ . The principle and details of the correction methodology are given in ref. (14) and we reiterate only the necessary parts here. A straight line fit to a set of  $N$  paired voxel values of MTR versus  $B_{1,\text{Error}}$  for a single specific tissue yields a gradient of  $k_{\text{spec}}$  and an intercept of  $\text{MTR}_0$  (14). Once  $k_{\text{spec}}$  and  $\text{MTR}_0$  are known for a single tissue, the general correction constant  $k$  can be calculated, and the entire MTR map, consisting of more than one tissue type, can thus be corrected for  $B_1$  variation in each individual voxel  $i$  using the expression

$$\text{MTR}_0^i = \frac{\text{MTR}^i}{1 + k B_{1,\text{Error}}^i} \quad [4]$$

where

$$k = k_{\text{spec}} / \text{MTR}_0 \quad [5]$$

The success of this correction scheme relies on the existence of a sufficiently linear relationship between  $\text{MTR}_{\text{Error}}$  and  $B_{1,\text{Error}}$  in a well-defined tissue type. Although this relationship has been modelled and verified experimentally for tissues in the brain, it has not been investigated previously for skeletal muscle. In order to verify that this correction scheme is applicable to muscle, we used a quantitative two-pool model of pulsed MT to investigate the relationship between  $\theta$  and MTR, incorporating recently measured qMT parameters of healthy muscle (16). The details of the qMT model are described elsewhere (17). In brief, the continuous-wave power equivalent approximation (17) was used to describe the observed signal after application of a Gaussian-shaped MT pulse with offset frequency  $\Delta$  applied with a repetition time TR, using a super-Lorentzian lineshape to describe the RF absorption profile of the bound proton pool and a Lorentzian lineshape to describe the absorption profile of the free pool

(17). There are six uniquely determined tissue-specific parameters required in this implementation of the model, and the parameters used for healthy skeletal muscle in this work are summarised in Table 1. The model was implemented in Mathematica 7 (Wolfram Scientific, Champaign, IL, USA).

The relationship between  $MTR_{Error}$  and  $B_{1,Error}$  for healthy muscle is plotted as the full line in Fig. 1 for an MT pulse with a nominal flip angle of  $500^\circ$ , a duration of 10 ms and  $\Delta = 1200$  Hz with  $TR = 65$  ms. In the range between  $\pm 30\%$   $B_{1,Error}$ , the relationship is linear to within 8%, indicating that the measured MTR of healthy muscle may indeed be corrected for  $B_1$  deviations using the scheme described above. In order to simulate the effects of variations in  $MTR_0$ , we also plotted this relationship for two different values of the bound pool transverse relaxation time,  $T_{2b} = 2$  and  $4 \mu s$ , shown as broken and dotted lines, respectively, in Fig. 1. Although it has not yet been determined which qMT parameters principally determine MTR changes in muscle disease,  $T_{2b}$  is altered here as a convenient way to simulate changes in MTR, supported by observations of alterations in this parameter in other conditions (18). The effect of varying  $T_{2b}$  in Fig. 1 illustrates that the relationship between  $MTR_{Error}$  and  $B_{1,Error}$  remains linear with a similar gradient despite different corresponding  $MTR_0$  values. Provided that a sufficiently large region of 'normal' muscle can be identified in order to determine  $k_{spec}^{normal}$ , the

generalised correction factor  $k$  is, in principle, also appropriate for correcting the whole skeletal muscle MTR map, where  $MTR_0$  may vary considerably as a result of disease.

In practice, the gradient  $k_{spec}$  and intercept  $MTR_0$  of a linear fit to  $MTR$  versus  $B_{1,Error}$  using  $N$  pairs of voxels may be determined employing standard analytical expressions given in refs. (14,19). In this work, we used these standard expressions and also extended the implementation to include estimates for the uncertainties on the fitted parameters, also employing analytical expressions (19) given by:

$$\sigma_{k_{spec}} = \sigma_{MTR} \sqrt{\frac{N}{\Gamma}}, \quad \sigma_{MTR_0} = \sigma_{MTR} \sqrt{\frac{\sum B_{1,Error}^2}{\Gamma}} \quad [6]$$

where

$$\sigma_{MTR} = \sqrt{\frac{1}{N-2} (MTR - MTR_0 - k_{spec} B_{1,Error})^2} \quad [7]$$

and

$$\Gamma = N \sum B_{1,Error}^2 - \left( \sum B_{1,Error} \right)^2 \quad [8]$$

Having reviewed the principle of the MTR correction scheme using  $B_{1,Error}$  maps, and investigated its applicability to skeletal muscle theoretically using a two-pool model of pulsed qMT, we next acquired MTR and  $B_1$  data in healthy subjects and patients in order to assess the performance of this correction scheme in practice.

### MR imaging parameters

Imaging was performed on a 3-T scanner (Siemens TIM Trio, Erlangen, Germany) operated with the body transmit coil. Subjects were positioned supine, feet first, and the signal from both lower limbs was received with a surface array placed over the lower limbs combined with the spine coil elements in the scanner bed.

An MT-weighted image ( $I_1$ ) was acquired with a three-dimensional fast low-angle shot (FLASH) readout ( $TR/TE = 68/3$  ms; flip angle,  $10^\circ$ ; matrix,  $256 \times 128 \times 40$ ; field of view,  $400 \times 200 \times 200$  mm<sup>3</sup>), preceded by a 10-ms Gaussian pulse with a nominal flip angle  $\theta_0$  of  $500^\circ$  and offset frequency  $\Delta$  of 1200 Hz. The sequence was repeated without the MT pulse to generate a second image  $I_0$ , and MTR was calculated using Equation [1]. Fifteen subjects were scanned with  $TR = 65$  ms.

$B_1$  variation was measured using the double-angle method (20). A turbo-spin-echo sequence ( $TR/TE = 7000/11$  ms; nominal excitation flip angle  $\alpha_1 = 60^\circ$ ; matrix,  $128 \times 60$ ;  $40 \times 10$ -mm slices; field of view,  $400 \times 200 \times 400$  mm<sup>3</sup>) was used to generate an initial image  $A_1$ . The sequence was repeated with an excitation flip angle  $\alpha_2 = 120^\circ$  to generate a second image  $A_2$ . Maps of the  $B_1$  fractional deviation from the nominal flip angle  $\alpha_1$  were calculated according to the relationship (20):

$$B_{1,dev} = \frac{\arccos\left(\frac{A_2}{2A_1}\right)}{\alpha_1} \quad [9]$$

and maps of  $B_{1,Error}$  were thus generated in percentage units as  $100 \times (B_{1,dev} - 1)$ .

An additional set of three, three-dimensional FLASH images ( $W_{\alpha_1, \alpha_2, \alpha_3}$ ) with variable nominal flip angles of  $\alpha_{1,2,3} = 5^\circ$ ,  $15^\circ$  and  $25^\circ$ , respectively, was acquired to generate a  $T_1$  map using

**Table 1.** Quantitative magnetisation transfer model parameters for the soleus muscle of the calf taken from ref. (16). In the model,  $R_b$  was set to  $1 s^{-1}$  and  $gM_0^a$  was set to unity. For details of the parameters and the model, see refs. (16,17)

Parameter	Value
$\frac{1}{R_a T_2^a}$	50.9
$\frac{f}{R_a(1-f)}$	0.15 s
$T_2^b$	5.93 $\mu s$
$RM_0^a$	17.0

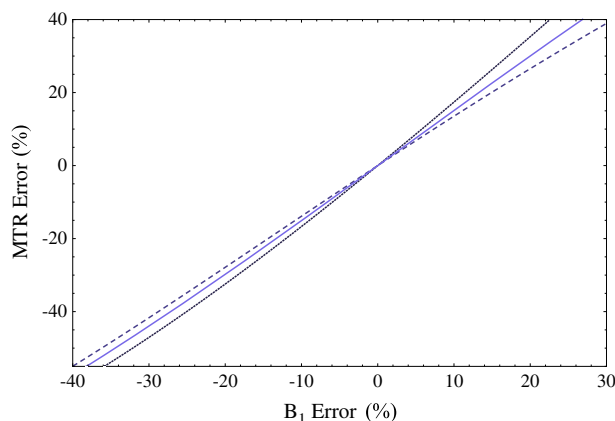


**Figure 1.** Simulation of the relationship between the magnetisation transfer ratio (MTR) error and  $B_1$  error using a quantitative two-pool model of pulsed MT demonstrating the approximately linear relationship between these quantities. The MTR error is evaluated at  $\theta_0 = 500^\circ$  and  $TR = 65$  ms. See Table 1 for the quantitative MT and pulse parameters used in the model.  $T_{2b} = 5.9 \mu s$  (full line),  $4 \mu s$  (broken line) and  $2 \mu s$  (dotted line). MT pulse parameters ( $\Delta = 1200$  Hz,  $\tau = 10$  ms Gaussian).

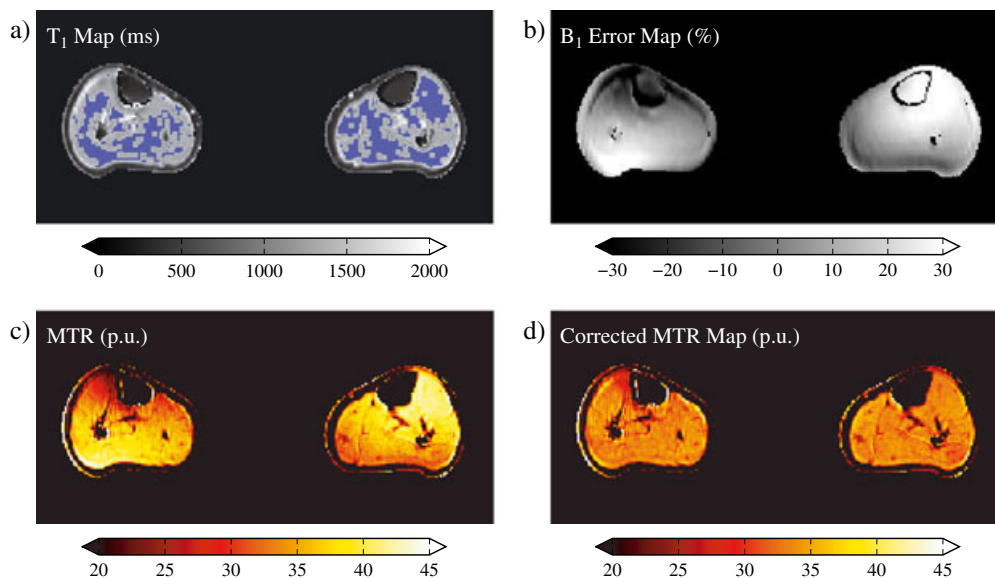


**Figure 2.** Summary of images used in the magnetisation transfer ratio (MTR) correction scheme from the lower legs of a healthy volunteer. (a)  $T_1$  map with the segmented and eroded normal muscle mask overlaid. (b)  $B_1$  map acquired using the double-angle method expressed as the percentage  $B_1$  error. (c) Raw MTR map before correction. (d) MTR map after correction displayed with the same window level as (c).

the so-called 'DESPOT-1' method in order to facilitate automatic segmentation of normal muscle (21) ( $TR/TE=23/3$  ms; matrix,  $256 \times 120 \times 80$ ; field of view,  $400 \times 200 \times 400$  mm<sup>3</sup>). The most heavily  $T_1$ -weighted image of the three ( $\alpha_3=25^\circ$ ) was also used as a reference for image registration and for the generation of masks for background thresholding and for drawing ROIs.

The total imaging time for MTR,  $B_1$  and  $T_1$  acquisitions in the thigh or calf was 11 min 38 s.

### Post-processing steps

Offline post-processing was performed for each individual subject using the Python scripting language under the Linux operating system as follows: the central 40 slices of the three images  $W_{\alpha 1, \alpha 2, \alpha 3}$  were selected to match the coverage of the MTR map, and the central 40 slices of the  $B_1$  map were selected to cover the same imaged volume. These MTR and  $B_1$  volumes, and  $W_{\alpha 1}$  and  $W_{\alpha 2}$ , were spatially registered to  $W_{\alpha 3}$  using the FLIRT tool in the FSL package (FMRIB, Oxford, UK) (22).

A  $T_1$  map was generated using the expression  $T_1 = TR / \ln(m)$ , where  $m$  is the gradient of a straight line fit to  $W_{1,2,3} / \sin \alpha_{1,2,3}$

versus  $W_{1,2,3} / \tan \alpha_{1,2,3}$  for each voxel in the set of three images  $W_{\alpha 1, \alpha 2, \alpha 3}$  (21). The three flip angles  $\alpha_{1,2,3}$  were corrected for  $B_1$  deviations in each voxel before calculation of the  $T_1$  map.

In order to identify regions of normal muscle that represented a single tissue type for the correction scheme, a binary mask representing the threshold range  $1200 < T_1 < 1600$  ms was generated, thereby selecting regions of muscle deemed to display 'normal' muscle  $T_1$  values (23,24) and to eliminate voxels containing purely fat, bone and fascia. In order to reduce partial volume effects at the boundaries between muscle, fascia and fat, the binary mask was eroded with a two-dimensional  $3 \times 3$  kernel. The normal muscle binary mask was applied to the MTR and  $B_{1, \text{Error}}$  maps, and the parameters  $k_{\text{spec}}$  and  $MTR_0$  were calculated by fitting to the data in this region. The whole unmasked MTR map was then corrected using the corresponding value of  $k$ .

The coefficient of variation of MTR ( $COV_{\text{MTR}}$ ) was calculated in the segmented muscle region before and after correction as the

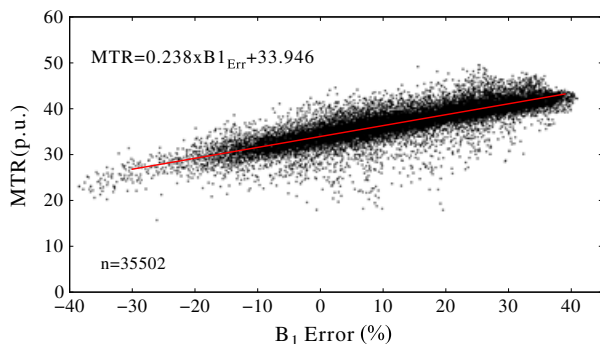


**Figure 3.** Plot of magnetisation transfer ratio (MTR) versus  $B_{1, \text{Error}}$  for normal muscle voxel values for the same subject as displayed in Fig. 2 (black points). The full line is a straight line fit to the data.

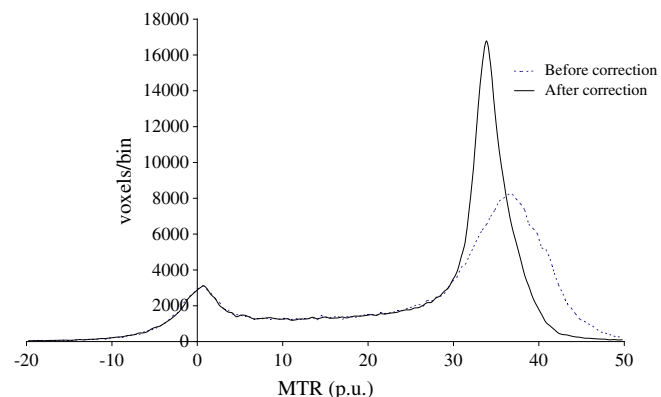


**Figure 4.** Whole-volume magnetisation transfer ratio (MTR) histogram of the healthy subject shown in Fig. 2 before (broken line) and after (full line) implementation of the correction scheme. The peak corresponding to skeletal muscle becomes narrower and is shifted to lower MTR values as a result of the correction. Negative MTR values arise from voxels containing subcutaneous fat and marrow.



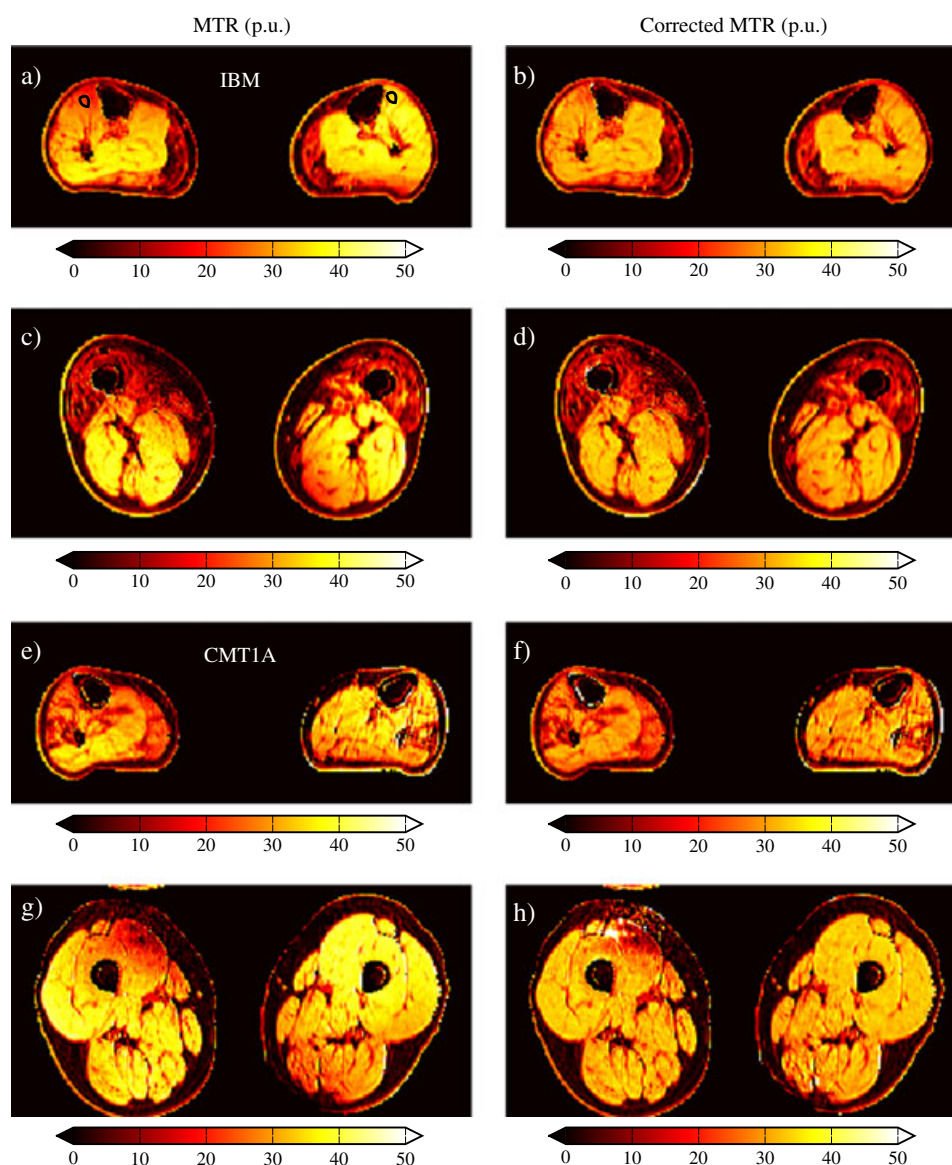


**Figure 5.** Magnetisation transfer ratio (MTR) maps before (left) and after (right) implementation of the correction scheme in the calf and thigh of patients with inclusion body myositis (IBM) (top) and Charcot-Marie-Tooth 1A (CMT1A) disease (bottom). In (a), two small regions of interest are overlaid to represent the location of measurements in the tibialis anterior muscles.

ratio of the MTR standard deviation  $\sigma$  to the MTR mean  $\mu$  of the voxels in that region:  $\text{COV}_{\text{MTR}} = \sigma/\mu$ . To evaluate the efficacy of the correction scheme on the whole MTR map, whole-volume MTR histograms were generated with a bin width of 0.5 p.u. Average histograms of all subjects in each of the two patient groups were calculated. In addition, in a subset of the first seven healthy individuals and first 10 patients, small irregular ROIs were drawn over the belly of the left and right tibialis anterior (TA) muscles on a single slice of the most  $T_1$ -weighted image  $W_{\alpha 3}$ , and translated onto the MTR maps to record the mean and standard deviation of the MTR in these muscles before and after correction for RF inhomogeneities.

#### Healthy volunteers and patients

Imaging data were acquired from the mid-calf and mid-thigh of 28 healthy volunteers (10 men, 18 women) with a mean age of

$40.6 \pm 16.8$  years (range, 22.0–88.0 years). The correction method was also evaluated in 12 patients with the inflammatory muscle disease inclusion body myositis (IBM) (25,26) (mean age,  $66.6 \pm 7.5$  years; range, 57.3–77.9 years; nine men, three women), chosen as a representative neuromuscular condition with muscle pathology known to include both oedematous inflammation and long-term fatty degeneration (27,28). Patients with IBM were diagnosed as either probable or definite IBM by accepted criteria (29). Eleven patients with genetically confirmed Charcot-Marie-Tooth disease type 1A (CMT1A) (30) were imaged (mean age,  $37.6 \pm 12.8$  years; range, 19.4–64.5 years; seven men, four women). CMT1A is an inherited peripheral neuropathy in which secondary muscle damage occurs as a result of neurogenic changes. All patients were recruited through consultants responsible for their care at the National Hospital for Neurology and Neurosurgery, London, UK, and the study was approved by the local ethical review board.

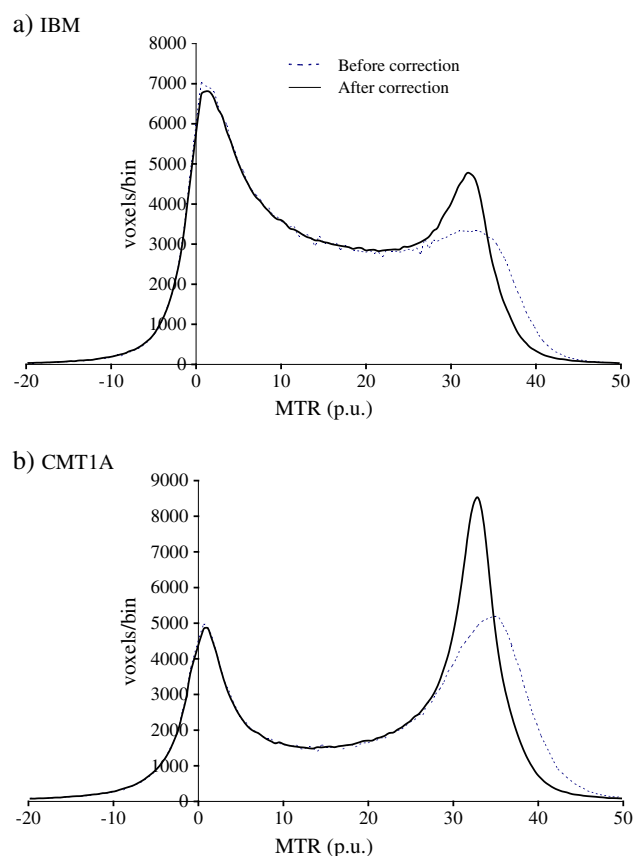


**Figure 6.** Average whole-volume magnetisation transfer ratio (MTR) histograms for the 12 patients with inclusion body myositis (IBM) (a) and the 11 patients with Charcot-Marie-Tooth 1A (CMT1A) disease (b) studied before (broken line) and after (solid line) implementation of the correction scheme. The correction can be seen to enhance the peaks corresponding to skeletal muscle in these patients.

## RESULTS

Examples of images from the lower legs of a healthy volunteer are shown in Fig. 2. The  $T_1$  map for this subject is shown in Fig. 2a with the automatically segmented normal muscle mask shown as an overlay. The accompanying  $B_1$  map, expressed in percentage units of the  $B_1$  error, is shown in Fig. 2b. Figure 2c shows the raw MTR map before any correction was applied. The window level is chosen to emphasise the characteristic MTR variations across the map. The corresponding MTR values of the segmented voxels are plotted *versus* the corresponding  $B_{1,\text{Error}}$  values in Fig. 3 and a linear fit is overlaid. In this example, there are 35502 voxels in the eroded segmented region of normal muscle and the corresponding values of  $k_{\text{spec}}$  and  $\text{MTR}_0$  are  $0.238 \pm 0.001$  and  $33.9 \pm 0.01$  p.u., respectively, leading to  $k = 7.0 \times 10^{-3}$ . The  $r^2$  coefficient of determination for this dataset is 0.750. The MTR map after correction using a value of  $k = 7.0 \times 10^{-3}$  is shown in Fig. 2d with the same window level as in Fig. 2c. The inhomogeneities in the MTR map can be seen to be reduced after correction.  $\text{COV}_{\text{MTR}}$  in the segmented muscle is reduced from 0.10 to 0.05 after correction in this example.

The whole-volume MTR histogram for the same subject before (broken line) and after (full line) correction is shown in Fig. 4. Two distinct peaks are seen in the shape of the histogram, corresponding principally to subcutaneous fat/marrow and skeletal muscle, respectively. The peak corresponding to the muscle becomes narrower and shifts to lower MTR values after correction. The mode value of the muscle peak is shifted from 36.8 to 33.9 p.u. after correction in this subject, and the peak interquartile width between the 25th and 75th percentiles, evaluated in the range between 20 and 50 p.u. to include principally muscle, was reduced from 7.4 to 4.0 p.u.

MTR maps of the lower legs and thighs before (left) and after (right) correction for patients with IBM (top) and CMT1A (bottom) are shown in Fig. 5. Histograms averaged over all

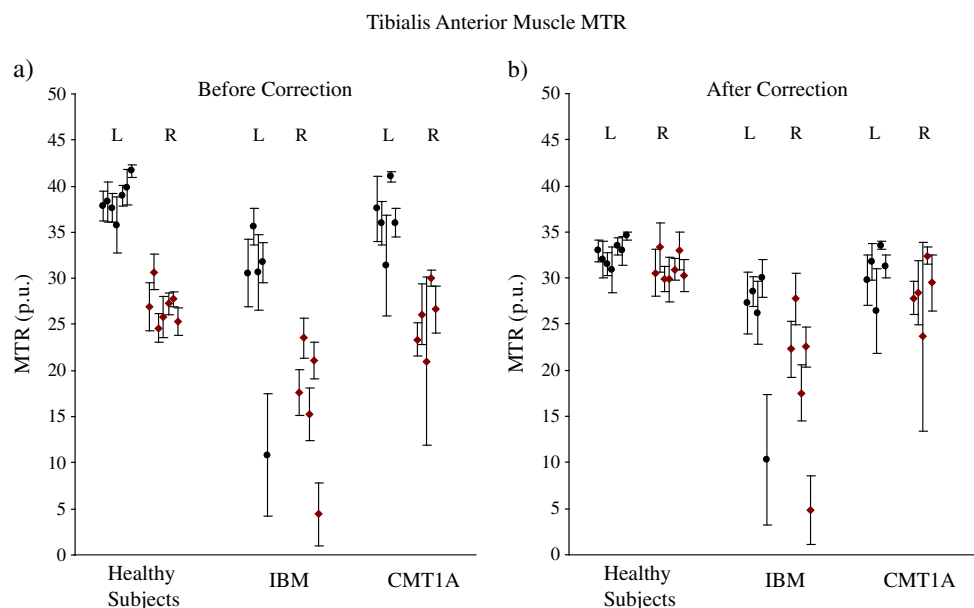


**Figure 7.** Mean magnetisation transfer ratio (MTR) in regions of interest (ROIs) in the left and right tibialis anterior (TA) muscles of a sample of seven healthy subjects and 10 patients. Error bars represent the standard deviation of the measured MTR in the ROI. Correcting for  $B_1$  inhomogeneities serves to reduce the left/right differences and better separate the patient groups from healthy subjects. CMT1A, Charcot-Marie-Tooth 1A; IBM, inclusion body myositis; L, left; R, right.

**Table 2.** Summary of correction scheme average parameters for the groups and anatomies studied. Magnetisation transfer ratios (MTRs) are for the segmented normal muscle only. The relative percentage reductions of the coefficient of variation (COV) are calculated as:  $100 \times [1 - (\text{COV}_{\text{After}}/\text{COV}_{\text{Before}})]$

		$k_{\text{spec}}$	$k \times 10^3$	MTR <sub>Before</sub> (p.u.)	MTR <sub>After</sub> (p.u.)	COV <sub>Before</sub>	COV <sub>After</sub>	% reduction	COV <sub>Before</sub>	COV <sub>After</sub>	% reduction
Volunteers ( <i>n</i> =28)	Calf	0.24±0.01	7.07±0.69	36.3±1.5	33.9±0.8	0.094	0.057	39.4	0.042	0.024	44.2
	Thigh	0.23±0.02	6.78±0.72	39.3±1.3	34.6±0.9	0.095	0.063	33.6	0.033	0.027	19.1
IBM ( <i>n</i> =12)	Calf	0.22±0.07	6.84±1.95	33.8±1.8	32.2±1.3	0.113	0.086	24.1	0.054	0.039	27.3
	Thigh	0.24±0.18	7.60±6.37	35.2±4.4	31.3±2.5	0.153	0.120	21.9	0.125	0.079	37.3
CMT1A ( <i>n</i> =11)	Calf	0.25±0.04	7.52±1.20	35.2±1.0	32.9±0.6	0.103	0.069	32.5	0.029	0.018	37.8
	Thigh	0.24±0.03	7.12±1.31	37.9±1.7	33.8±1.3	0.108	0.082	23.7	0.044	0.039	11.9

CMT1A, Charcot-Marie-Tooth disease type 1A; IBM, inclusion body myositis.

patients in each group are shown before (broken line) and after (full line) correction in Fig. 6. An equivalent shift in the histogram muscle peaks can be observed in the patient groups. The mode peak position was shifted from 35.4 to 33.9 p.u. in IBM and from 34.9 to 32.9 p.u. in CMT1A; the interquartile widths were reduced from 8.9 to 7.4 p.u. in IBM and from 7.9 to 5.5 p.u. in CMT1A.

The results of the ROI analysis in a small subset of patients and healthy individuals are presented in Fig. 7. Mean MTR in the left and right TA muscles is shown before and after application of the correction scheme, with error bars depicting the MTR standard deviation in the ROI. The correction scheme eliminates most of the apparent left/right differences in TA MTR of healthy subjects, and enables better separation of the patient groups from healthy individuals.

Table 2 summarises the fitted values of  $k_{\text{spec}}$  and  $k$  for the lower leg and thigh muscles of the three groups studied. MTR values in the normal segmented muscle before and after correction are also given. COV<sub>MTR</sub> values evaluated using the normal muscle are also given in Table 2, together with the relative reduction in variation before and after correction.

## DISCUSSION

The purpose of this work was to evaluate, in theory and practice, the suitability of correcting skeletal muscle MTR maps with  $B_1$  data using an established correction scheme, and to determine whether doing so reduces variation caused by instrumental imperfections in MTR measurements in neuromuscular disease.

The results shown in Fig. 2c and 2d demonstrate a substantial qualitative increase in the homogeneity of muscle MTR maps in a healthy subject by applying the correction scheme. This reduction in variability is supported by reduced COVs in the normal muscle tissue of healthy subjects and by reductions in the peak width and mode values of whole-volume muscle MTR histograms (Table 2 and Fig. 4). The shape of the peak corresponding to normal muscle in the MTR histograms is consistently altered after correction, showing a reduced width and shift in peak position to lower MTR values (Fig. 4). The influence of instrumental inhomogeneities in the  $B_1$  field on the MTR map is apparently reduced, allowing more of the genuine individual variability to be determined.

An important aspect of any image processing methodology is that it is applicable to patient groups in which considerable intra- and inter-subject variation caused by disease may be present. In the two patient groups studied here, the correction scheme

produced qualitatively visible adjustments in the MTR maps (Fig. 5), as well as reducing the variation between subjects and shifts in peak positions in MTR histograms (Table 2, Fig. 6) and ROIs (Fig. 7). It is likely that this correction will strengthen the correlations between measured MTR and clinical indices expected to exist in these patient groups, although this must still be demonstrated in future studies. Substantial reductions in the within- and between-subject standard deviations and COVs after applying the correction scheme are evident in Table 2. Reductions in the inter-subject variability as a result of correction for  $B_1$  effects have the benefit of more clearly revealing pathological changes that might otherwise be masked by RF inhomogeneities.

The correction scheme cannot adjust for regions of  $B_1$  variation so severe that there may be no remaining MR signal. This is particularly apparent in regions of the anterior medial right thigh in all subjects, in which there is a consistent region of signal drop-out in the vicinity of the vastus medialis muscle (Figs 5 and 8). This effect is a combination of the  $B_1$  variation affecting the imaging sequence excitation angle and the MT pulse amplitude. Nonetheless, in the areas immediately surrounding this region of signal drop-out, the right thigh MTR maps show somewhat reduced inhomogeneity after application of the  $B_1$  correction. It cannot be argued, however, that this is sufficient to allow confident inclusion of the right vastus medialis in quantitative analysis: signal loss caused by  $B_1$  variation in this region has been consistently noted on our scanner on a number of different sequences and contrast regimes. This issue requires further research, with particular consideration of the limb separation imposed by the geometry of the receiving coils (31).

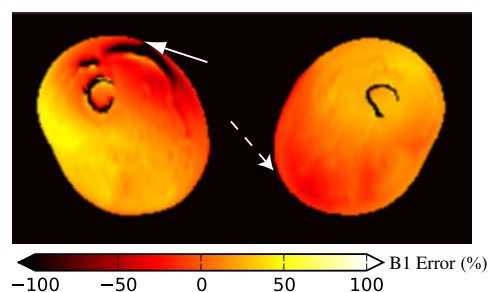


**Figure 8.** Map of the  $B_1$  error in the thigh of a volunteer. The anterior medial portion of the right limb consistently suffers the largest deviations from the prescribed  $B_1$  field (white arrow). The posterior medial portion of the left limb is symmetrically affected (broken arrow). The subject was scanned in the feet-first orientation.

The spatial variation of the  $B_1$  field observed in this study is reasonably consistent across all subjects. The region of lowest actual flip angle occurs in the right anterior calf muscles, often coinciding with the TA muscle (Fig. 2b). The field variation has circular diagonal symmetry, resulting in  $B_1$  values that are also lower than the nominally prescribed amplitude in the left posterior calf on the opposite side of the  $B_1$  map. On this basis, we propose that caution must be employed in attributing any observed MTR variation in these regions to genuine biological differences in both patients and healthy subjects if  $B_1$  variations have not been explicitly measured (4). A similar circular variation is observed in the thigh, where the lowest  $B_1$  field is measured in the medial anterior region of the right thigh and the highest  $B_1$  field is measured in the posterior medial region in the left thigh on the opposite side of the map (Fig. 8). It is worthwhile to note that these patterns of flip angle variation in the  $B_1$  map are reversed by scanning subjects in the head-first orientation, consistent with the expectation that  $B_1$  variation is principally caused by stationary patterns of the polarised RF field interacting with the particular anatomical geometry of the lower limbs and pelvis (31).

There are a number of different approaches to  $B_1$  mapping available (32), including the double-angle method, actual flip angle imaging (33), phase-sensitive methods (34), fitting to a signal null (35) and echo planar imaging-based methods. Evaluation of the relative merits of these methods is ongoing (32) and no method can provide an absolute measurement of the  $B_1$  field. The double-angle method was chosen in this work because it is one of the simplest to implement on a clinical system. The double-angle method is a two-dimensional spin-echo method and is therefore not ideal for correcting three-dimensional FLASH data because of the necessary differences in spatial coverage and the additional effects of slice selection that are not present in three-dimensional imaging. A three-dimensional  $B_1$  mapping sequence, such as actual flip angle imaging or signal nulling, may be considered more appropriate in this context. However, as the authors of ref. (14) noted, the requirements for the  $B_1$  map in this MTR correction scheme are relatively relaxed for successful determination of the coefficients for correction and, indeed, a  $B_1$ -weighted sequence may be sufficient for this purpose.

The normal muscle segmentation employed here using  $T_1$  maps is fully automatic, meaning that the *post hoc* correction can be applied with minimal user input, potentially allowing automatic offline processing in the context of a large study and reducing observer bias. However, in the few most severe clinical cases, there is very little or no remaining 'normal' muscle from which to determine the MTR correction coefficients. This can result in failure of the segmentation routine in regions comprising a very small number of voxels, potentially introducing systematic bias into fitted parameters. In these cases, some supervision of the routine may be necessary in order to manually define a region around suitably identified normal muscle or to establish that there is no remaining normal tissue with which to perform a correction.

The use of  $T_1$  maps for segmentation in this work offers a convenient means of identifying normal muscle tissue. However, this method may be theoretically susceptible to bias in a scenario in which muscle tissue displays 'normal'  $T_1$  relaxation properties, but already shows pathology-related changes in the MT behaviour. Other MRI modalities with different contrasts may be used for segmentation employing threshold- or histogram-based

approaches (36), although inhomogeneities in the magnitude of the MRI signal can make this process difficult to implement robustly. The suitability of  $T_1$  mapping for this purpose will be determined more fully with future investigation of the MT properties of 'normal appearing' muscle in  $T_1$  images and maps.

The potential clinical applicability of the correction method is further demonstrated by the ROI analysis of the TA muscles shown in Fig. 7. The principal apparent systematic variations in TA MTR in healthy subjects are largely removed by correction with the  $B_1$  data, and the distribution of TA MTRs in the patients is somewhat reduced whilst retaining the principal pathological alterations in the MTR values. Such region-of-interest-based analyses are likely to remain useful as an initial approach to analysing quantitative muscle MR data in future clinical studies.

In order to evaluate the applicability of the correction method in the context of clinical trials, it will be necessary to establish that the reduction in artefactual MTR inhomogeneities strengthens the association between measured MTR and clinical measures, such as muscle strength (7). The MTR methods must also be demonstrated to be reproducibly sensitive to disease over timescales of some months or years. We are currently evaluating several methods, including MTR map correction, in large-scale patient investigations with correlative clinical data recorded longitudinally. It is also anticipated that such MTR correction schemes could be of value in multi-centre trials by reducing the instrumentally dependent muscle MTR variability from scanners at different collaborating centres (14).

## CONCLUSIONS

In this work, we have shown by both theoretical modelling and practical evaluation in healthy volunteers and representative patient groups that skeletal muscle MTR maps may be corrected for RF inhomogeneities using  $B_1$  mapping data. We have shown that the correction scheme reduces spatial inhomogeneities in muscle MTR and reduces apparent inter-subject variation. The method therefore shows promise for further improving the pathological sensitivity of MTR measurements in neuromuscular conditions, where there is a growing need for sensitive, quantitative imaging markers of disease.

## Acknowledgements

C.D.J.S. is grateful to Mark J. White for valuable technical advice and to Enrico De Vita and Robert Janiczek for useful discussions.

This work was funded by the Medical Research Council (MRC) through the MRC Centre for Neuromuscular Diseases, University College London (UCL) Institute of Neurology. M.M.R. receives support from the Muscular Dystrophy Campaign. This work was undertaken at UCLH/UCL who received a proportion of funding from the Department of Health's NIHR Biomedical Research Centres funding scheme.

## REFERENCES

1. Mercuri E, Pichiecchio A, Allsop J, Messina S, Pane M, Muntoni F. Muscle MRI in inherited neuromuscular disorders: past, present, and future. *J. Magn. Reson. Imaging* 2007; 25: 433–440.
2. Koltzenburg M, Yousry T. Magnetic resonance imaging of skeletal muscle. *Curr. Opin. Neurol.* 2007; 20: 595–599.
3. Henkelman RM, Stanisz GJ, Graham SJ. Magnetization transfer in MRI: a review. *NMR Biomed.* 2001; 14: 57–64.



4. Schwenzer NF, Martirosian P, Machann J, Schraml C, Steidle G, Claussen CD, Schick F. Aging effects on human calf muscle properties assessed by MRI at 3Tesla. *J. Magn. Reson. Imaging* 2009; 29: 1346–1354.
5. Mattila KT, Komu ME, Koskinen SK, Niemi PT. Exercise-induced changes in magnetization transfer contrast of muscles. *Acta Radiol.* 1993; 34: 559–562.
6. Zhu XP, Zhao S, Isherwood I. Magnetization transfer contrast (MTC) imaging of skeletal muscle at 0.26Tesla – changes in signal intensity following exercise. *Br. J. Radiol.* 1992; 65: 39–43.
7. Sinclair CDJ, Morrow JM, Miranda MA, Davagnanam I, Cowley PC, Mehta H, Hanna MG, Koltzenburg M, Yousry TA, Reilly MM, Thornton JS. Skeletal muscle MRI magnetisation transfer ratio reflects clinical severity in peripheral neuropathies. *Journal of Neurology Neurosurgery and Psychiatry*. 2011 DOI: 10.1136/jnnp.2011.246116
8. Boss A, Martirosian P, Küper K, Fierlbeck G, Claussen CD, Schick F. Whole-body magnetization transfer contrast imaging. *J. Magn. Reson. Imaging*, 2006; 24: 1183–1187.
9. McDaniel JD, Ulmer JL, Prost RW, Franczak MB, Jaradeh S, Hamilton CA, Mark LP. Magnetization transfer imaging of skeletal muscle in autosomal recessive limb girdle muscular dystrophy. *J. Comput. Assist. Tomogr.* 1999; 23: 609–614.
10. Elskamp I, Knol DL, Vrenken H, Karas G, Meijerman A, Filippi M, Kappos L, Fazekas F, Wagner K, Pohl C, Sandbrink R, Polman CH, Uitendhaag BM, Barkhof F. Lesional magnetization transfer ratio: a feasible outcome for remyelinating treatment trials in multiple sclerosis. *Multiple Sclerosis*, 2010; 16: 660–669.
11. Horsfield MA, Barker GJ, Barkhof F, Miller DH, Thompson AJ, Filippi M. Guidelines for using quantitative magnetization transfer magnetic resonance imaging for monitoring treatment of multiple sclerosis. *J. Magn. Reson. Imaging*, 2003; 17: 389–397.
12. Volz S, Nöth U, Rotarska-Jagiela A, Deichmann R. A fast  $B_1$ -mapping method for the correction and normalization of magnetization transfer ratio maps at 3T. *Neuroimage*, 2010; 49: 3015–3026.
13. Henkelman RM, Huang X, Xiang QS, Stanisz GJ, Swanson SD, Bronskill MJ. Quantitative interpretation of magnetization transfer. *Magn. Reson. Med.* 1993; 29: 759–766.
14. Ropele S, Filippi M, Valsasina P, Korteweg T, Barkhof F, Tofts PS, Samson R, Miller DH, Fazekas F. Assessment and correction of  $B_1$ -induced errors in magnetization transfer ratio measurements. *Magn. Reson. Med.* 2005; 53: 134–140.
15. Samson R, Wheeler-Kingshott C, Symms M, Tozer D, Tofts P. A simple correction for  $B_1$  field errors in magnetization transfer ratio measurements. *Magn. Reson. Imaging*, 2006; 24: 255–263.
16. Sinclair CD, Samson RS, Thomas DL, Weiskopf N, Lutti A, Thornton JS, Golay X. Quantitative magnetization transfer in vivo healthy human skeletal muscle at 3T. *Magn. Reson. Med.* 2010; 64: 1739–1748.
17. Ramani A, Dalton C, Miller DH, Tofts PS, Barker GJ. Precise estimate of fundamental in-vivo MT parameters in human brain in clinically feasible times. *Magn. Reson. Imaging*, 2002; 20: 721–731.
18. Tozer D, Ramani A, Barker GJ, Davies GR, Miller DH, Tofts PS. Quantitative magnetization transfer mapping of bound protons in multiple sclerosis. *Magn. Reson. Med.* 2003; 50: 83–91.
19. Taylor J. *An Introduction to Error Analysis: The Study of Uncertainties in Physical Measurements*. University Science Books: Sausalito, Ca; 1997.
20. Stollberger R, Wach P. Imaging of the active  $B_1$  field in vivo. *Magn. Reson. Med.* 1996; 35: 246–251.
21. Deoni SCL, Rutt BK, Peters TM. Rapid combined  $T_1$  and  $T_2$  mapping using gradient recalled acquisition in the steady state. *Magn. Reson. Med.* 2003; 49: 515–526.
22. Smith SM, Jenkinson M, Woolrich MW, Beckmann CF, Behrens TEJ, Johansen-Berg H, Bannister PR, De Luca M, Drobnjak I, Flitney DE, Niazy RK, Saunders J, Vickers J, Zhang Y, De Stefano N, Brady JM, Matthews PM. Advances in functional and structural MR image analysis and implementation as FSL. *Neuroimage*, 2004; 23: S208–S219.
23. Gold GE, Han E, Stainsby J, Wright G, Brittain J, Beaulieu C. Musculoskeletal MRI at 3.0T: relaxation times and image contrast. *Am. J. Roentgenol.* 2004; 183: 343–351.
24. Stanisz GJ, Odobina EE, Pun J, Escaravage M, Graham SJ, Bronskill MJ, Henkelman RM. T-1, T-2 relaxation and magnetization transfer in tissue at 3T. *Magn. Reson. Med.* 2005; 54: 507–512.
25. Griggs RC, Askanas V, DiMauro S, Engel A, Karpati G, Mendell JR, Rowland LP. Inclusion body myositis and myopathies. *Ann. Neurol.* 1995; 38: 705–713.
26. Machado P, Miller A, Holton J, Hanna M. Sporadic inclusion body myositis: an unsolved mystery. *Acta Reumatol. Port.* 2009; 34: 161–182.
27. Briani C, Doria A, Sarzi-Puttini P, Dalakas MC. Update on idiopathic inflammatory myopathies. *Autoimmunity*, 2006; 39: 161–170.
28. Karpati G, O'Ferrall EK. Sporadic inclusion body myositis: pathogenic considerations. *Ann. Neurol.* 2009; 65: 7–11.
29. Needham M, Mastaglia FL. Inclusion body myositis: current pathogenic concepts and diagnostic and therapeutic approaches. *Lancet Neurol.* 2007; 6: 620–631.
30. Reilly MM, Shy ME. Diagnosis and new treatments in genetic neuropathies. *J. Neurol. Neurosurg. Psychiatry*, 2009; 80: 1304–1314.
31. Storey P, Lee VS, Sodickson DK, Santoro D, Zhang B, Lim RP, Atanasova IP, Stoffel DR, Chen Q, Wiggins GC.  $B_1$  inhomogeneity in the thigh at 3T and implications for peripheral vascular imaging. *Proceedings of the 17th Annual Meeting ISMRM*, Honolulu, HI, USA, 2009; 426.
32. Lutti A, Hutton C, Helms G, Finsterbusch J, Weiskopf N. Optimization and group comparison of RF ( $B_1$ ) mapping methods at 3T. *Proc. Int. Soc. Magn. Res. Med.* 2009; 17: 2796.
33. Yarnykh VL. Actual flip-angle imaging in the pulsed steady state: a method for rapid three-dimensional mapping of the transmitted radiofrequency field. *Magn. Reson. Med.* 2007; 57: 192–200.
34. Morrell GR. A phase-sensitive method of flip angle mapping. *Magn. Reson. Med.* 2008; 60: 889–894.
35. Dowell NG, Tofts PS. Fast, accurate, and precise mapping of the RF field in vivo using the  $180^\circ$  signal null. *Magn. Reson. Med.* 2007; 58: 622–630.
36. Mattei JP, Fur YL, Cuge N, Guis S, Cozzone PJ, Bendahan D. Segmentation of fascias, fat and muscle from magnetic resonance images in humans: the DISPIMAG software. *MAGMA*, 2006; 19: 275–279.